Science Advances

AAAS

advances.sciencemag.org/cgi/content/full/3/9/e1701186/DC1

Supplementary Materials for

Ultrahigh mobility and efficient charge injection in monolayer organic thin-film transistors on boron nitride

Daowei He, Jingsi Qiao, Linglong Zhang, Junya Wang, Tu Lan, Jun Qian, Yun Li, Yi Shi, Yang Chai, Wei Lan, Luis K. Ono, Yabing Qi, Jian-Bin Xu, Wei Ji, Xinran Wang

Published 6 September 2017, *Sci. Adv.* **3**, e1701186 (2017)
DOI: 10.1126/sciadv.1701186

This PDF file includes:

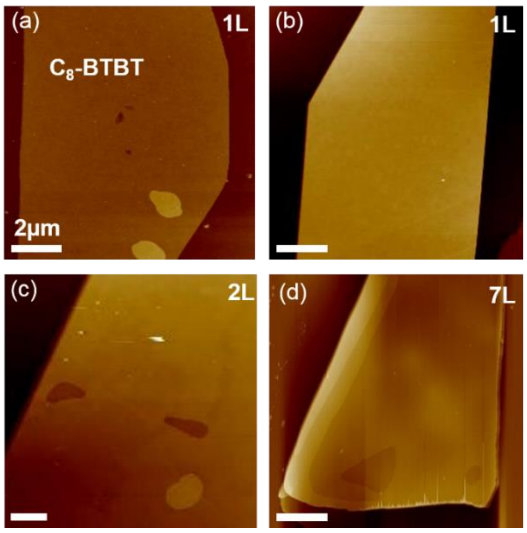

fig. S1. AFM images of several representative C_8-BTBT thin films on BN with different thickness.

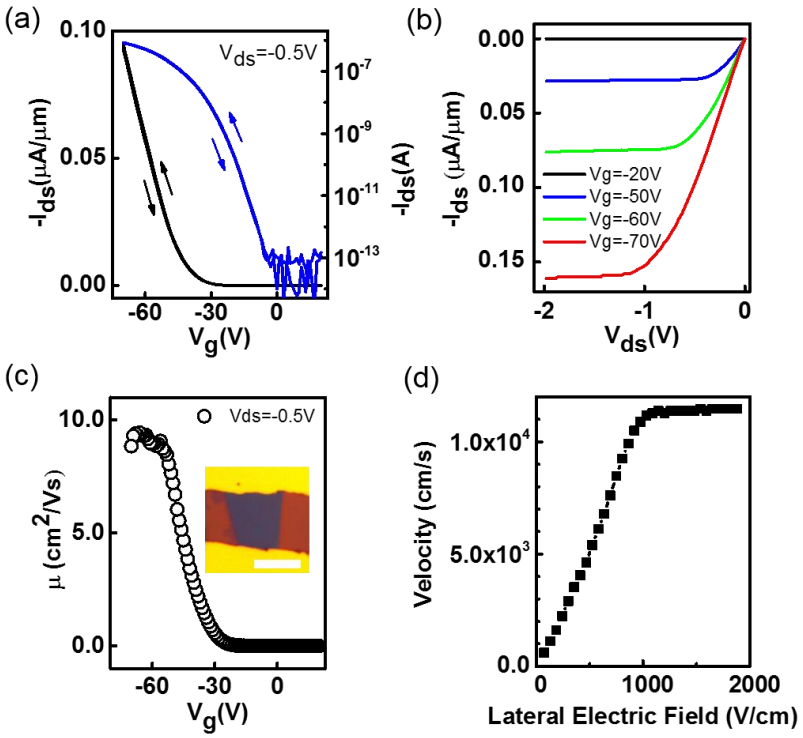

fig. S2. A two-terminal monolayer C_8-BTBT OTFT. (**a**) Room temperature double sweep I_{ds}-V_g characteristics with linear scale (left) and log scale (right). (**b**) I_{ds}-V_{ds} characteristics at room temperature. (**c**) Extrinsic mobility extracted in the linear regime. Inset shows the optical micrograph of the device. Scale bar, 10 μm. (**d**) Carrier velocities as a function of Lateral Electric Field.

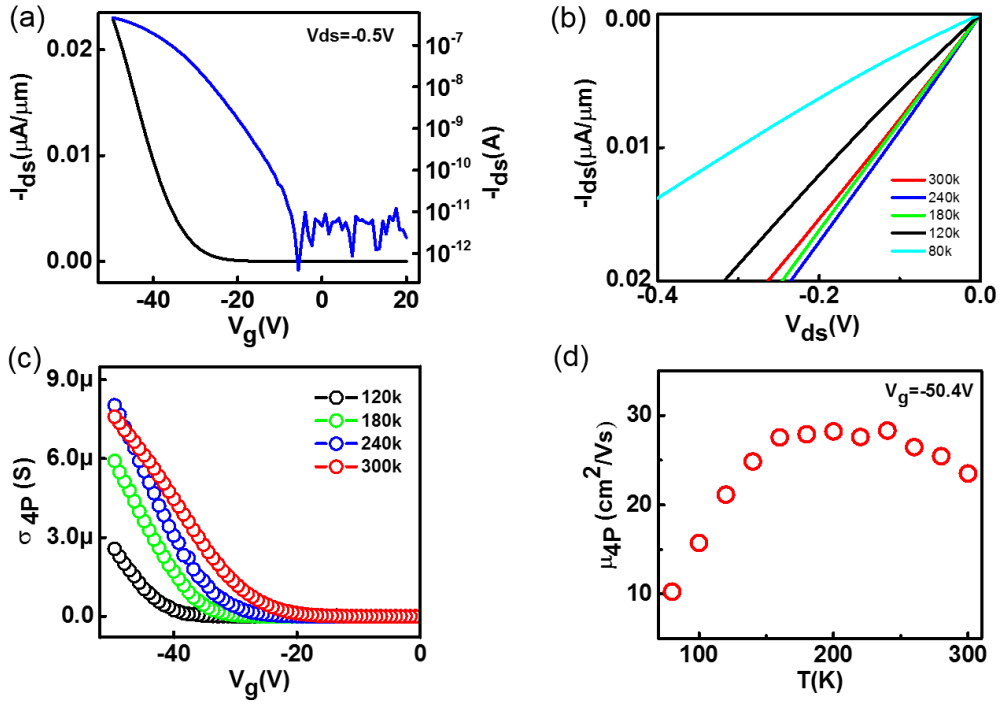

fig. S3. Electrical data of another four-probe monolayer C8-BTBT OTFT. (**a**) Room temperature I_{ds}-V_g characteristics with linear scale (left) and log scale (right). (**b**) Low-bias I_{ds}-V_{ds} characteristics under different temperature. (**c**) Channel conductance $\sigma_{4P} \sim V_g$ under different temperature. (**d**) μ_{4P} as a function of temperature under V_g = -50.4V.

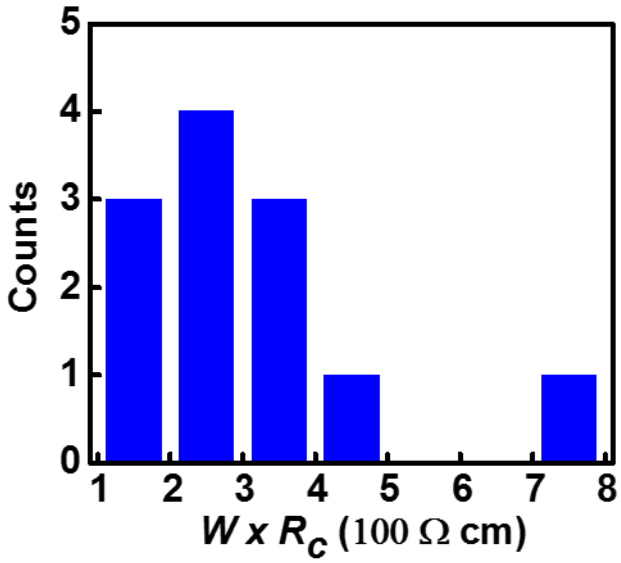

fig. S4. Histogram of contact resistance of 12 monolayer C8-BTBT OTFTs. The contact resistance is derived under V_g=-70V, V_{ds}=-0.3V.

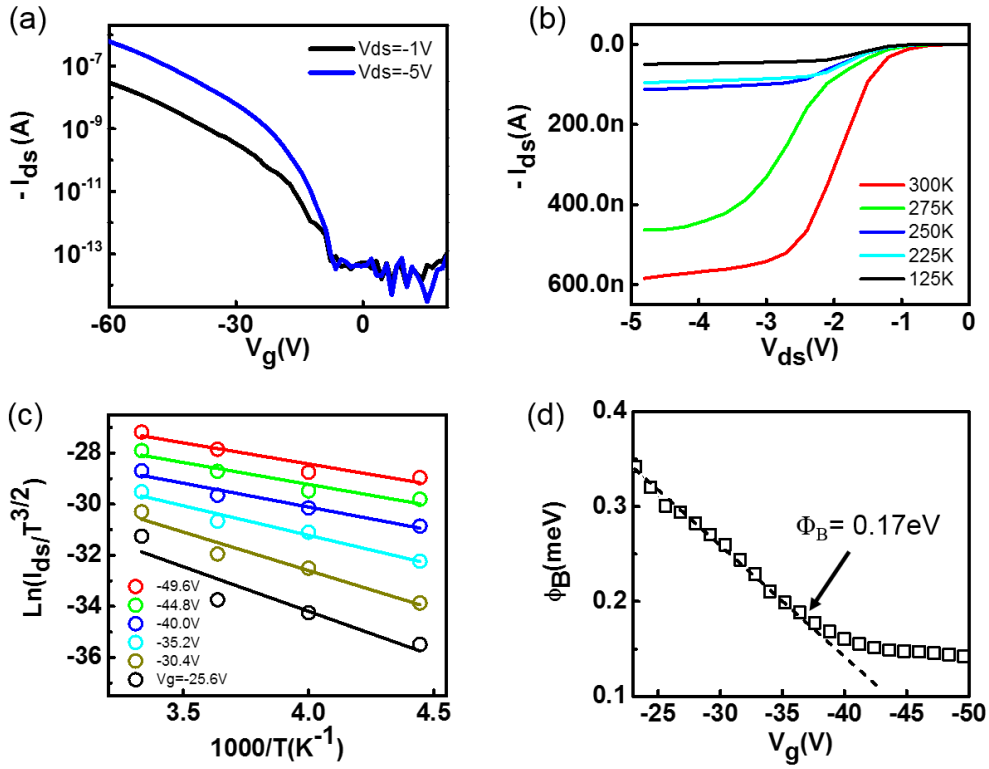

fig. S5. Electrical data of another bilayer C_8-BTBT OTFT. (**a**) Room-temperature I_{ds}-V_g characteristics (log scale) at different bias. (**b**) I_{ds}-V_{ds} characteristics (V_g = -60V) under different temperatures. (**c**) Arrhenius plot of $ln(I_{ds}/T^{3/2})$ under V_{ds} = -1V. (d) The SB height as a function of V_g derived from (c).

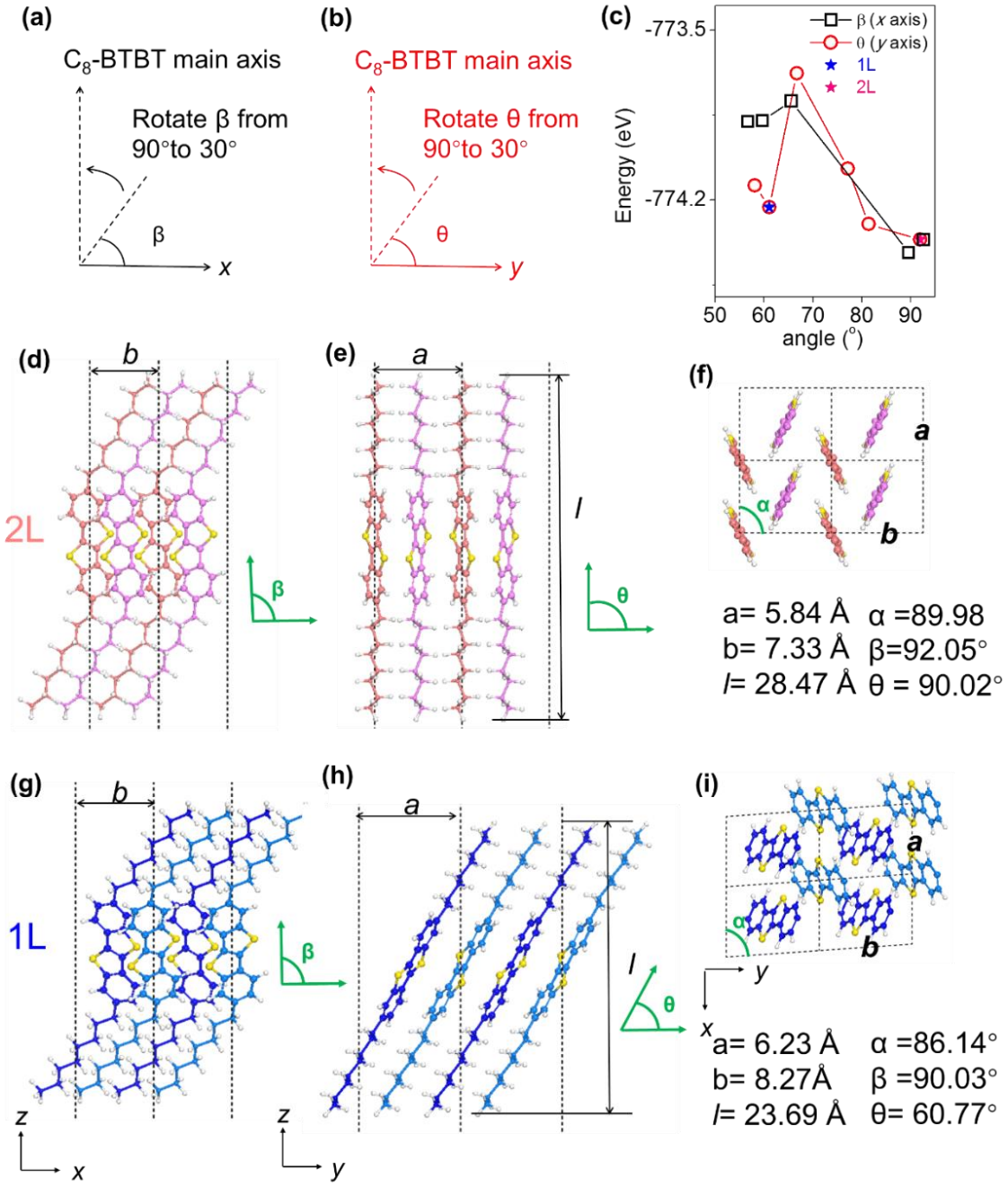

fig. S6. We investigated 14 configurations through rotating β and θ angle of C_8-BTBT molecules from 90° to 30° along the *x* and *y* axis, respectively. The schematics are shown in (**a** to **b**). (**c**) The relationship of total energy and *β/θ* angle for fully relaxed monolayer structures. The configurations rotated along *y* is more stable than that rotated along *x*. The configurations of 1L and 2L are determined by comparing the relationship between energy and *θ* angle. We determine that *θ* of 1L and 2L C_8-BTBT are close to 60° and 90°, respectively. The configurations of 1L and 2L are marked as blue and red stars. (**d** to **f**) Geometric structures of 2L in side view along *x* (d), along *y* (e) and top view along *x*-*y* plane (f). (**g** to **i**) Geometric structures of 1L in side view along *x* (g), along *y* (h) and top view along *x*-*y* plane (i). Detailed lattice parameters of 2L and 1L are shown on panel (f) and (i), respectively.

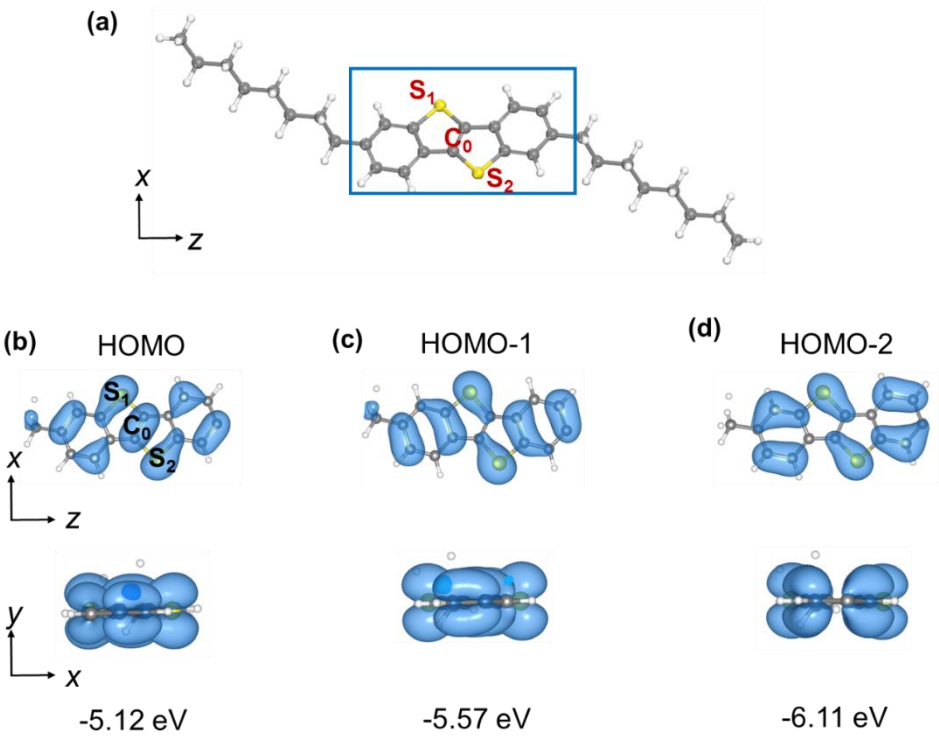

fig. S7. Geometric structure of single C_8-BTBT molecule and visualized wave functions. (**a**) Geometric structure of single C_8-BTBT molecule. Visualized wavefunctions for HOMO (**b**), HOMO-1 (**c**) and HOMO-2 (**d**) states, which contributed by the atoms in blue rectangle of panel (a). Here, two sulfur atoms are defined as S_1 and S_2. Two carbon atoms between S_1 and S_2 are defined as C_0.

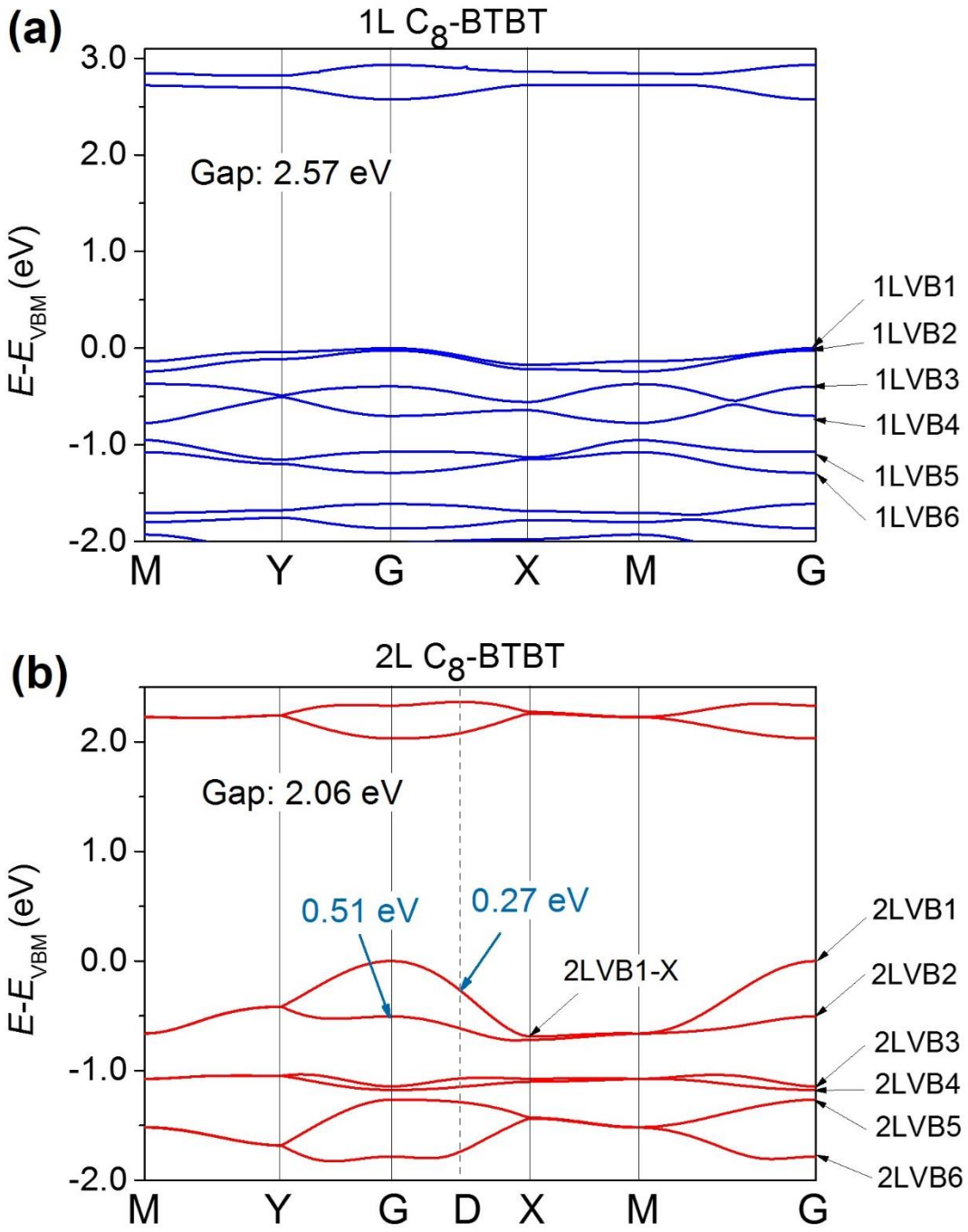

fig. S8. Electronic band structures of 1L and 2L C_8-BTBT. Electronic band structures of 1L (**a**) and 2L (**b**) C_8-BTBT. 1L and 2L are both semiconductors with 2.57 eV and 2.06 eV G-point direct bandgap. Six states of valence bands at G-point are marked on the 1L (1LVB1 ~ 1LVB6) and 2L (2LVB1 ~ 2LVB6) band structures, respectively.

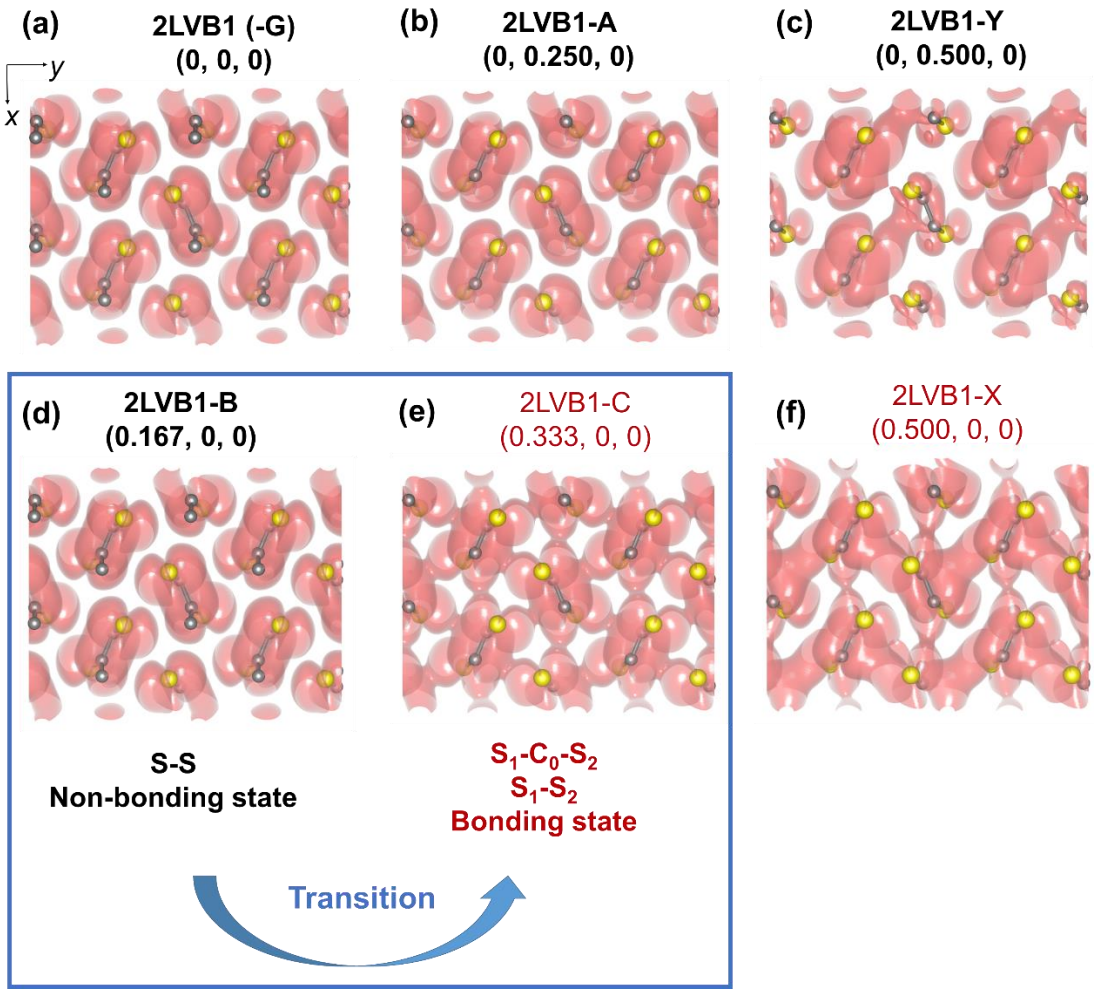

fig. S9. Visualized wave functions for six states in the momentum space of the highest valence band of 2L C_8-BTBT. Visualized wave functions for six states in the momentum space of the highest valence band of 2L-C_8-BTBT at G-point (0, 0, 0) (**a**), A point (0, 0.250, 0) (**b**), Y point (0, 0.5, 0) (**c**), B point (0.167, 0, 0) (**d**), C point (0.333, 0, 0) (**e**) and X point (0.5, 0, 0) (**f**). Therein, 2LVB1-G, 2LVB1-A, 2LVB1-Y and 2LVB1-B are non-bonding states of S atoms. 2LVB1-C and 2LVB1-X are bonding states derived from hybridization between S-S and S-C atoms. **In other words, a transition from non-boning state to bonding state arises along G-X directions.** The critical point of this transition is around half G-X path, at D (0.25 0 0) point.

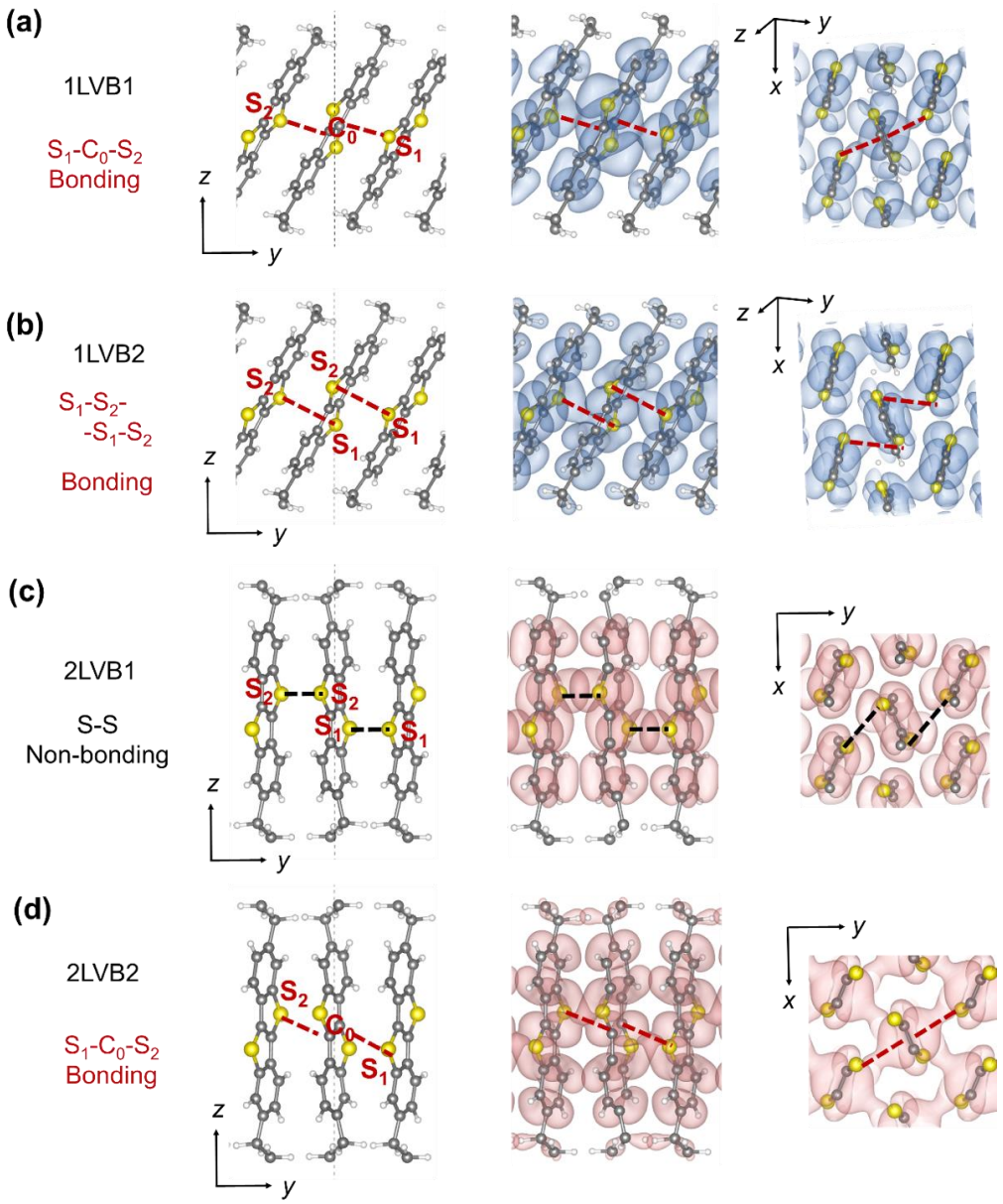

fig. S10. Visualized G-point wave functions for VB1 and VB2 of 1L and 2L in *yz* and *xy* (top view of thiophene part) planes, respectively. Visualized G-point wave functions for VB1 and VB2 of 1L (**a** to **b**) and 2L (**c** to **d**) in *yz* and *xy* (top view of thiophene part) planes, respectively. The states are marked in band structures of 1L and 2L (**fig. S8**). VB1 and VB2 states derive from HOMO orbitals of single C_8-BTBT molecules. Only the orbitals from the four atoms including two S (S_1 and S_2) and two C atoms (C_0) in C_8-BTBT molecule involved in hybridizations. In 1L C_8-BTBT, two intermolecular bonding states (1LVB1 and 1LVB2) were formed with wave function overlap of two adjacent molecules through S_1-C_0-S_2 and S_1-S_2--S_1-S_2 interactions as shown in (a) and (b), respectively. **1LVB1 and 1LVB2 states are both bonding states and share a very small energy difference (0.02 eV).** In 2L C_8-BTBT, 2LVB2 (d) is a bonding state with the wave function overlap of S_1-C_0-S_2, which is similar with that of 1LVB1. However, for 2LVB1 (c), the stand-up configuration of 2L results in the *p* orbitals of the S atoms of two adjacent molecules parallel approaching, which leads to the orbitals repulsing each other, but not hybridizing into bonding states. Localized 2LVB1 state **develops a ~0.5 eV higher energy level with 2LVB2 (bonding states).**

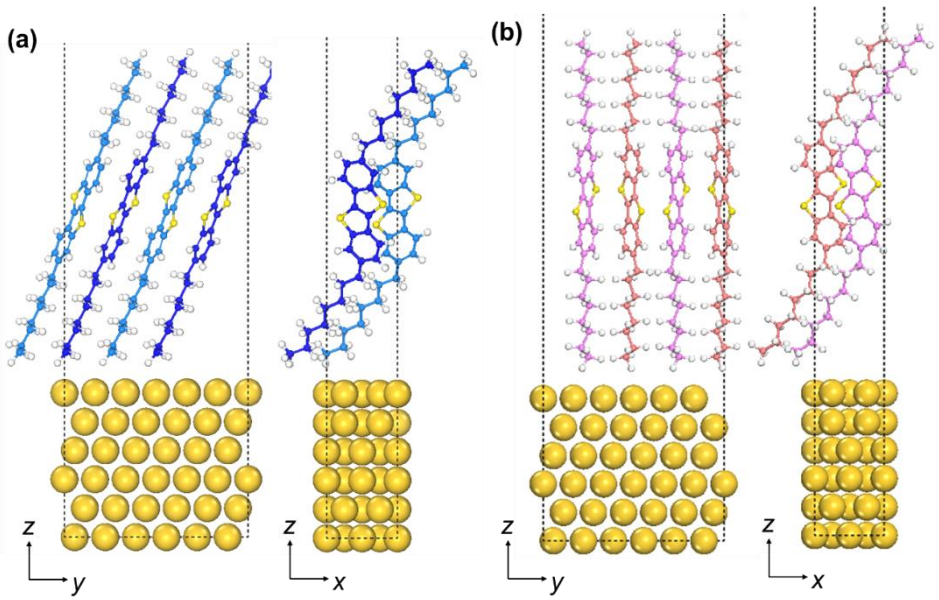

fig. S11. The contact models of Au electrodes with 1L or 2L C_8-BTBT. The contact models of Au electrodes with 1L (**a**) or 2L (**b**) C_8-BTBT. A 1×2 supercell C_8-BTBT and 6L $\begin{pmatrix} 2 & 0 \\ 3 & 6 \end{pmatrix}$ Au (111) surface are included. Two kinds of Au configurations are built, the lattice constants of which are kept as Au (111) (a=5.88 Å, b= 15.29 Å) or the same as C_8-BTBT (see fig. S6) equilibrium lattice constants, respectively. Figure S11 (a) and (b) show the contact geometries, in which the lattice constant of Au was slightly expended and compressed to fit the lattices of 1L and 2L C_8-BTBT, respectively. The gap between Au and 1L/ 2L C_8-BTBT are 2.59/2.57 Å, respectively. The relative energy levels between Au and 1L/2L C_8-BTBT share <0.1 eV difference between two models. The band-alignment diagram determined by the model kept as the lattice constants of C_8-BTBT is shown in Figure 4.

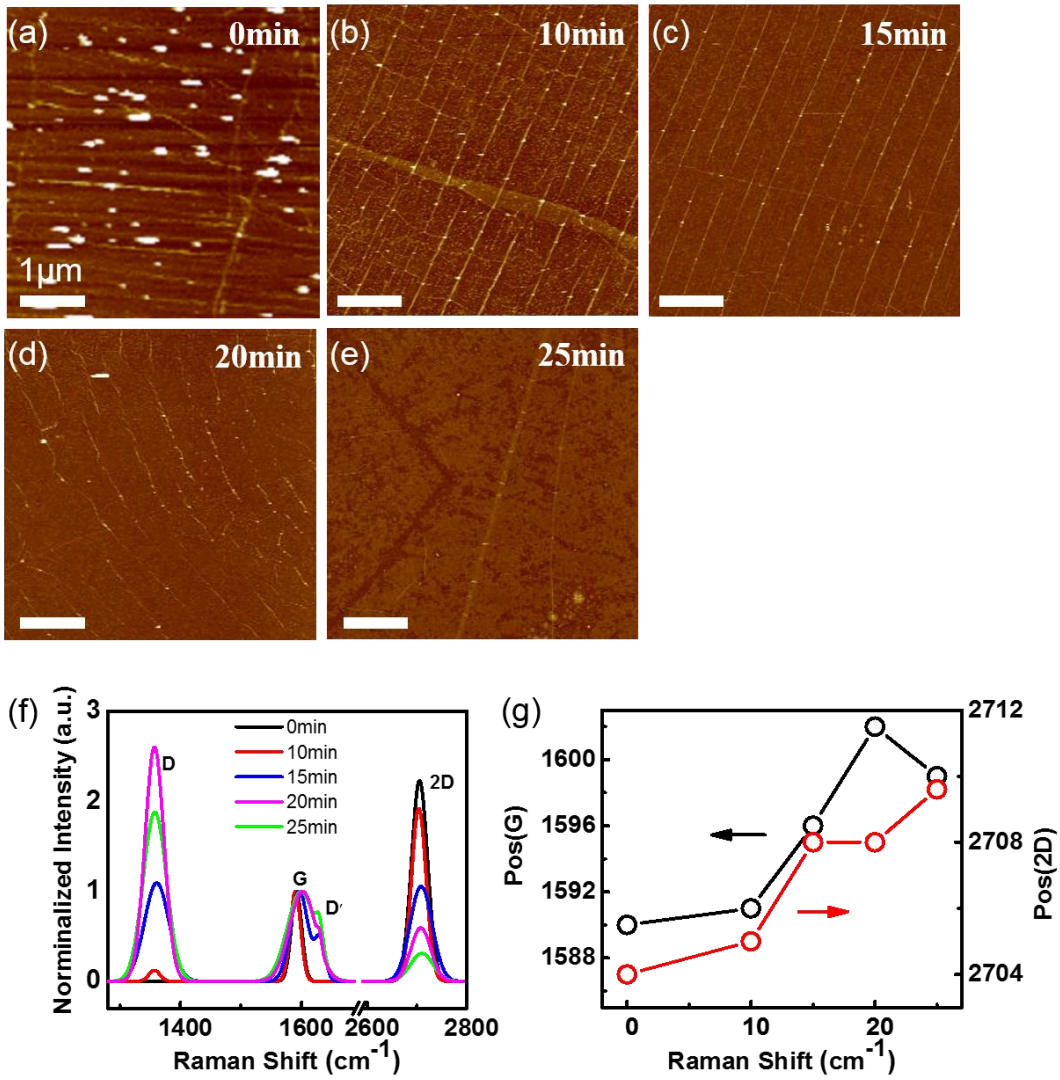

fig. S12. Characterizations of CVD graphene. (**a** to **e**) AFM images of CVD graphene undergone UVO for 0, 10, 15, 20 and 25 minutes, respectively. We found that graphene became discontinuous if we exposed them in UVO for more than 20 minutes. The 20-minute sample showed the best contact with C_8-BTBT. (f) Normalized intensity Raman spectra of the CVD graphene under different UVO time. The strong D band and a smaller D' band appearred after 15 minutes UVO exposure. The intensity ratio of 2D/G decreased with increasing UVO time, and the both G and 2D band showed blue shift. By Lorentzian fitting, we extracted the positions of G and 2D bands as function of UVO time (g).

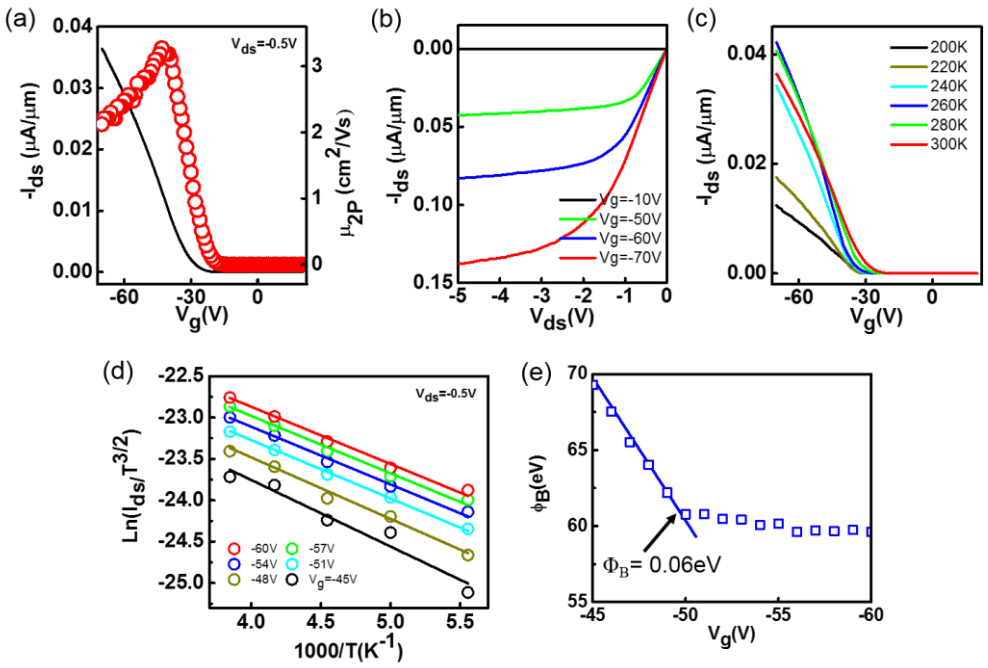

fig. S13. Electrical data of another graphene-contacted bilayer C_8-BTBT OTFT. Room temperature transfer (**a**) and output (**b**) characteristics. The extracted extrinsic mobility is also plotted in (a). (**c**) Transfer characteristics at different temperature of the same device in (a). The current increases initially with cooling down to 260K, and then decreases due to contact effect. (**d**) Arrhenius plot of $ln(I_{ds}/T^{3/2})$ under V_{ds} = -0.5V. (**e**) The SB height as a function of V_g derived from (d).